6-17-2010

Computational Analysis of Binary Segregation During Colloidal Crytallization with DNA-mediated Interactions

Raynaldo T. Scarlett
University of Pennsylvania, scarlet3@seas.upenn.edu

John C. Crocker
University of Pennsylvania, jcrocker@seas.upenn.edu

Talid Sinno
University of Pennsylvania, talid@seas.upenn.edu

Computational Analysis of Binary Segregation During Colloidal Crytallization with DNA-mediated Interactions

Abstract

A detailed computational study of compositional segregation during growth of colloidal binary solid-solution crystals is presented. Using a comprehensive set of Metropolis Monte Carlo simulations, we probe the influence of colloid size, interaction strength, and interaction range on the segregation process. The results are interpreted in terms of a simple, but descriptive mechanistic model that allows us to connect to studies of binary segregation in atomic systems. The validity of Metropolis Monte Carlo simulations for the nonequilibrium phenomena investigated in this work is established theoretically and by connections to Brownian dynamics and molecular dynamics simulations. It is demonstrated that standard Metropolis Monte Carlo, properly applied, can provide an efficient framework for studying many aspects of crystallization in colloidal systems.

Disciplines

Biochemical and Biomolecular Engineering | Chemical Engineering | Engineering

Computational analysis of binary segregation during colloidal crystallization with DNA-mediated interactions

Raynaldo T. Scarlett, John C. Crocker, and Talid Sinno[a)]

Department of Chemical and Biomolecular Engineering, University of Pennsylvania,
220 S. 33rd St., Philadelphia, Pennsylvania 19104, USA

A detailed computational study of compositional segregation during growth of colloidal binary solid-solution crystals is presented. Using a comprehensive set of Metropolis Monte Carlo simulations, we probe the influence of colloid size, interaction strength, and interaction range on the segregation process. The results are interpreted in terms of a simple, but descriptive mechanistic model that allows us to connect to studies of binary segregation in atomic systems. The validity of Metropolis Monte Carlo simulations for the nonequilibrium phenomena investigated in this work is established theoretically and by connections to Brownian dynamics and molecular dynamics simulations. It is demonstrated that standard Metropolis Monte Carlo, properly applied, can provide an efficient framework for studying many aspects of crystallization in colloidal systems. © *2010 American Institute of Physics.* [doi:10.1063/1.3453704]

I. INTRODUCTION

Colloidal models have provided considerable insight into a variety of fundamental processes related to particle aggregation including crystal nucleation,[1,2] morphology,[3] melting,[4] and growth.[1,3] By virtue of their size (from nanometers to microns) and well-defined interactions, colloidal models can provide useful platforms for probing subtle mechanistic elements related to aggregation in atomic systems.[5–7] In addition to serving as a model system, colloidal assembly technology is now sufficiently versatile and controllable to provide a host of promising approaches for fabricating novel materials with useful properties (e.g., optical metamaterials[8]).

The assembly of colloidal crystals using engineered interparticle interactions has now been demonstrated experimentally with a variety of particle types and sizes. There are numerous approaches for engineering interactions between colloidal particles including direct particle modification[9,10] and induction by external fields.[11] Examples of interparticle interaction sources that have been successfully realized in experiments include depletion[12] and electrostatic[13] and magnetic[14] fields. One versatile route for colloidal assembly relies on the use of grafted brushes comprised of single-stranded DNA oligomers, as shown schematically in Fig. 1. In this approach, the single-stranded DNA sequences are engineered to either be partially self-complementary[10,15] or to be partially complementary to another "linker" oligomer that is introduced into the solution containing the engineered particles.[9,12] Both approaches have been shown to drive colloidal crystallization under the appropriate conditions of the total particle volume fraction, system temperature relative to the DNA melting point, and particle size relative to the DNA oligomer length.[16] A key advantage of DNA-mediated inter-

actions is their specificity, which, in principle, enables a systematic approach for fabricating multicomponent assemblies with an arbitrary number of different particle "types." Recent efforts in this regard have led to the assembly of binary colloidal and nanoparticle crystals with controllable composition and even compositional ordering.[17–19]

Much theoretical emphasis has been placed on the prediction of equilibrium phase diagrams for assembly as a function of interparticle interaction characteristics,[20,21] while relatively little consideration has been directed toward growth kinetics and the related problem of defect formation. Numerous literature studies have sought to increase the range of accessible assembly structures by manipulating particle shape,[22] preassembling building blocks with desired symmetries,[23] and theoretically predicting interaction models that would lead to interesting assemblies.[20] Nonetheless, it is generally well understood that the incorporation of particles into a growing crystal is controlled by both thermodynamic and kinetic factors at the crystal interface.[17,24,25] For example, recent theoretical[26,27] and experimental[10,16,17] studies highlight the importance of the growth kinetics for realizing high-quality DNA-colloidal assemblies that are consistent with the predicted equilibrium phase.

In this paper, we extend a recent study of the growth of binary solid-solution (close-packed) colloidal crystals in which particle assembly is driven by DNA-mediated interactions.[17] Our motivation arises from recent experimental work that suggests the importance of kinetics in the growth of colloidal crystals, with concomitant implications for defect formation.[16] We analyze the effect of growth kinetics on the binary segregation process at the crystallization interface using a model that is closely connected to an actual experimental system.[9,12,16,17] Using detailed Metropolis Monte Carlo (MMC), and now also Brownian dynamics (BD) and molecular dynamics (MD) simulations, we construct simple mechanistic models to describe the process of

[a)]Author to whom correspondence should be addressed. Electronic mail: talid@seas.upenn.edu.
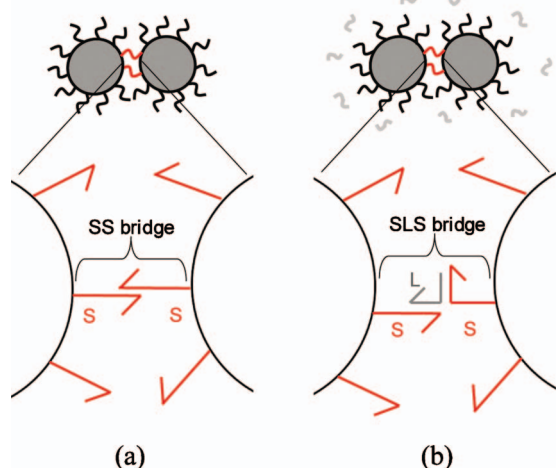
132, 234705-1

FIG. 1. Schematic representation of two variants of DNA-mediated colloidal assembly systems in which particles are modified by grafting DNA oligomers onto their surfaces. (a) Direct bridge system. (b) Linker-mediated system. S=spacer oligomer and L=linker oligomer.

interfacial segregation that appears to be generically applicable to a broad variety of materials systems. We also make direct connections between colloidal and atomistic binary systems and explore in detail the application of MMC simulation to the study of nonequilibrium crystal growth phenomena. The remainder of the paper is outlined as follows. In Sec. II, we provide brief details of the experimental system upon which the present study is based and the associated pair potential model used in the simulations. In Sec. III, we describe the various simulation methods employed. Results and associated discussion are presented in Sec. IV. In Sec. V, the MC results are further interpreted in the context of BD and MD simulations, and finally, conclusions are presented in Sec. VI.

II. BINARY SOLID-SOLUTION CRYSTALLIZATION WITH DNA-MEDIATED INTERACTIONS

The experimental system on which the present computational study is based consists of two mixed populations of micron-sized (diameter, $\sigma=0.98$ μm) polystyrene spheres, A and B, which bear short grafted strands of single-stranded DNA oligomers, whose sequences differ by a single nucleotide.[17] Pairs of particles interact with each other according to the scheme shown in Fig. 1(b), i.e., via linker DNA molecules that are introduced into the solution and which are designed to be partially complementary to the single-stranded DNA molecules on the particle surfaces. Experimental details regarding the DNA grafting procedure and particle fabrication are given in Ref. 12. Here, we note simply that the interactions between two A particles are assumed to be stronger than those between one A and one B and between two B particles, i.e., $E_b^{AA} > E_b^{AB} > E_b^{BB}$, where E_b^{XY} is the maximum value of the DNA-induced sphere-sphere binding energy. Based on simple thermodynamic considerations, this interaction system is expected to form close-packed A-rich crystals, with some minority concentration of B particles inserted randomly into the lattice (further details are provided in Sec. IV B).
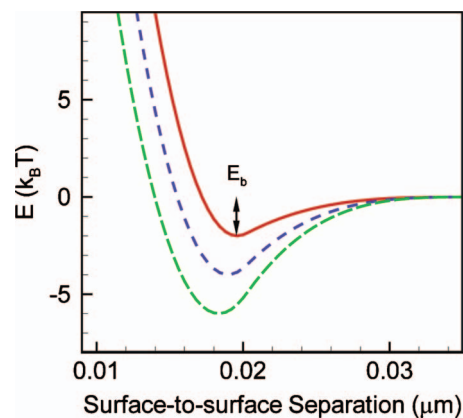

FIG. 2. DNA-mediated pair potential used in this study for several different values of the binding strength. Solid line—$E_b=2.0k_BT$, short-dashed line—$E_b=4.0k_BT$, and long-dashed line—$E_b=6.0k_BT$.

A quantitative model for the effective pair potential between two microspheres was developed recently.[9] The pair interaction potential between two spherical colloids is given generically by the function $E(h)=E^r(h)+E^a(h)$, where h is the particle separation, $E^r(h)$ is a short-ranged repulsion due to compression of the grafted DNA coils, and $E^a(h)$ represents attraction due to the formation of an equilibrium number of DNA bridges between strands on neighboring particles. Expressions for both components of this interaction model were derived in Ref. 9. Here, we express these functions schematically as

$$\frac{E^r(h)}{k_B T} \sim f(h) \tag{1}$$

and

$$\frac{E^a(h)}{k_B T} \sim -g(h)e^{(\Delta G/k_B T)}, \tag{2}$$

where $f(h)$ and $g(h)$ are functions that describe the distribution of the ends of the grafted strands versus height above the particle surface and ΔG is the total hybridization free energy for a single DNA bridge (see Ref. 9 for details). In all ensuing discussions, the binding strength E_b^{XY} is defined as the minimum of $E(h)$ for any two spheres, X and Y. Example plots of the pair potential function we use are shown in Fig. 2 for several different values of E_b^{XY}. Note that the binding energy depends exponentially on the system temperature and free energy change for hybridization of the linker and the two grafted strands, as shown in Eq. (2), leading to a very strong temperature dependence of the binding energy. This is in stark contrast to potentials representing atomic systems in which the binding energy is essentially independent of temperature. Due to this temperature dependence, the range for crystal formation is typically only about 0.5 °C.[9]

III. SIMULATION METHODOLOGY

Both MMC and BD simulations were performed to study the binary crystal growth process using the pair potential described in Sec. II. For both types of crystal growth simulations, a periodic cubic simulation cell containing 5000 randomly distributed, nonoverlapping particles[28] at a prescribed

volume fraction ϕ (where $\phi \sim 0.1-0.4$) was allowed to relax to constant average energy at a prescribed temperature and volume (constant NVT ensemble). For a given run, the temperature was fixed at a value that provided the desired interaction well depths according to the potential function specified in Refs. 9 and 17 so that $3.0k_BT < E_b^{AA} < 6.0k_BT$ and $0.4k_BT \leq \Delta E_b \leq 1.5k_BT$ where $\Delta E_b \equiv E_b^{AA} - E_b^{AB}$.

For all interaction strengths and system volume fractions considered in our study, a metastable fluid phase was obtained following relaxation of the initial random particle positions because of the large free energy barrier associated with crystal nucleation.[29] Once the fluid was equilibrated, a spherical close-packed (fcc) crystallite containing 30–150 particles was inserted into the center of the equilibrated fluid (replacing an equal number of fluid particles). All seed sizes were chosen to ensure that the seeds were larger than the critical size under the particular system conditions. The system was allowed to further relax while keeping the seed particles fixed. When the surrounding fluid was equilibrated with the fixed seed, the seed particles were released and the entire system was allowed to further evolve without constraints. The criterion for seed equilibration was based on the number of solidlike particles identified in the seed; once this number reached the initial seed size, the seed was deemed to be equilibrated. Note that solid particles were identified using a local bond order analysis first outlined in Ref. 30 and later applied by Frenkel and co-workers.[2,31] This choice of method for identification of seed-fluid equilibrium is based on the observation that the bond order parameter used here requires extensive ordering of the fluid around a crystallite before the surface particles in the crystallite are identified as solid particles. Thus, when the seed is initially introduced into the fluid, the order parameter fails to identify the surface seed particles as solid until the fluid is equilibrated around the crystalline seed. Using the initialization procedure described here, the nucleation barrier against crystallization is circumvented, allowing us to focus on a single growing crystallite. During the course of each simulation, particles were periodically identified as solid or fluid, and the cluster size was noted.

A. MMC and BD simulation details

As noted above, both MMC and BD simulations were used to study colloidal crystallization. We discuss the connections between MMC and BD simulations later; here we present briefly the salient details for each. We employed standard MMC with a Verlet neighbor list implementation.[32] Individual MC moves were performed by displacing randomly selected particles with a uniformly distributed random vector with maximum magnitude rd_{max} in each spatial dimension. Move attempts were accepted and rejected according to the standard Metropolis criterion. Particle assignment to either a solid or a fluid state was performed every 100 moves/particle, or sweeps.

The BD simulations were performed using the algorithm of van Gunsteren and Berendsen,[33] which numerically integrates the Langevin equation

$$m_i \dot{v}_i(t) = -m_i \gamma_i v_i + F_i + R_i, \tag{3}$$

where γ_i, v_i, and F_i are the frictional (damping) coefficient, velocity, and systematic force acting on the ith colloid, respectively. R_i represents a random, stationary stochastic force acting on particle i that arises from interactions with the solvent molecules. Hydrodynamic interactions between particles were neglected in all BD simulations.

Note that the stochastic force $R(t)$ is assumed constant over the integration interval Δt, and therefore the correlation time for $R(t)$ is $O(\Delta t)$. Thus, in order to generate the required stationary Markovian process during the numerical integration of the Langevin equation, the constraint, $\Delta t \ll \gamma^{-1}$, must be obeyed, setting a limit on the size of the time step that can be employed in the BD simulations (in addition to that imposed by the accuracy of any given numerical integration scheme). Finally, we note that in the limit $\gamma \equiv 3\pi\eta\sigma \rightarrow 0$, the BD algorithm in Ref. 33 can be simplified to the Verlet MD algorithm,[32] where the implicit solvent viscosity is now $\eta \sim 0$ and purely inertial dynamics are present.[33]

IV. RESULTS AND DISCUSSION

A. Simulating crystal growth "dynamics" with MMC

Generally, crystal growth from a surrounding supersaturated fluid proceeds by diffusion to the crystal surface, followed by the dynamic processes of particle attachment and detachment from the surface. The overall crystal growth process can be characterized by two time scales: the time scale of the crystal growth and the diffusion time scale to the crystal front. The growth time scale for a monolayer of crystal is given by $\tau_{growth} = \sigma/(dr/ds)$, where dr/ds is the radial growth rate, s is the number of MMC sweeps, and σ is the particle diameter. Note that the sweep count s serves as the MC measure of time in the following analysis.

Generally speaking, the diffusion timescale is given by $\tau_{diff} = L(s)^2/D$, where $L(s)$ is the (time-dependent) diffusion length scale of the concentration profile around the growing crystal and D is the bulk fluid diffusion coefficient. We determine the diffusion length scale by considering the diffusion problem around a growing (spherical) crystallite of radius $R(s)$ within the quasistatic (or pseudosteady state) assumption, whereby it is assumed that the fluid density profile around the growing cluster is rapidly established relative to the growth rate of the crystal. Under this assumption, the particle volume fraction profile in the fluid is given by

$$\phi(r,s) = \phi_b\left(1 - \frac{R(s)}{r}\right) + \frac{R(s)\phi_s}{r}, \tag{4}$$

where ϕ_b and ϕ_s are the volume fractions in the fluid bulk and at the crystallite surface. The latter represents the vapor pressure of the crystallite, which is finite when the particle dissociation rate is nonzero.

The density profile in Eq. (4) leads to the classical result that the diffusion boundary layer around a growing crystal is of the same order as the crystal diameter and therefore is time dependent. However, it is possible to establish conditions in simulation where the effective diffusion length scale
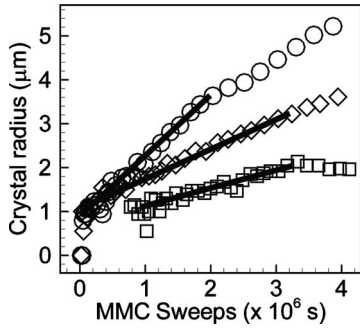
FIG. 3. Radial growth rate as a function of MMC sweeps for several different operating conditions showing linear regime, followed by decreasing rate due to fluid depletion. $\sigma = 0.98$ μm for all cases.

can be made constant, thus simplifying the analysis. Consider a particle balance over the growing crystal, i.e.,

$$\frac{dn}{ds} = \beta n^{2/3} J(s; \phi, E_b), \tag{5a}$$

where β is a geometric factor that depends on the crystallite shape and $J(s; \phi, E_b)$ is the particle arrival flux at the crystal surface. Under the assumption of spherical crystallite geometry, the radius of a growing crystal is defined as $r = (\sigma/2) n^{1/3} \phi_{\mathrm{crys}}^{-1/3}$, where ϕ_{crys} is the volume fraction of the crystal and n is the number of colloids in the growing crystallite. Using this expression for the radius in Eq. (5a) gives

$$\frac{dr}{ds} = (\sigma/6) \beta J(s; \phi, E_b) \phi_{\mathrm{crys}}^{-1/3} \equiv A(s). \tag{5b}$$

Note that under conditions where the arrival flux is constant, the radial growth rate is also a constant. As shown in Fig. 3, the radial growth rate for a single-component crystal obtained from example MMC simulations with several different values for overall volume fraction ϕ and particle binding energy E_b indeed exhibits linear behavior after a short initial transient, indicating that the arrival flux is constant during this time. This behavior stems from the relatively small simulation box (with periodic boundary conditions), which effectively limits the growth of a density boundary layer around the growing crystallite. For example, the length of a cubic box containing 5000 particles at $\phi = 0.3$ is only two to three times the diameter of a spherical crystallite containing 200–300 particles. At long simulation times in Fig. 3, the fluid density becomes appreciably depleted, which leads to a continuous reduction in the arrival flux and hence the crystal growth rate.

The preceding considerations suggest that a constant diffusion length scale (and hence time scale) can be defined for the portion of the simulation over which the radial growth rate is constant. For convenience, we choose the particle diameter as a length scale so that $\tau_{\mathrm{diff}} = \sigma^2 / D$. A dimensionless crystal growth rate Γ_D can then be defined as the ratio of τ_{diff} to τ_{growth}, i.e.,

$$\Gamma_D \equiv \frac{\tau_{\mathrm{diff}}}{\tau_{\mathrm{growth}}} = \frac{(dr/ds)\sigma}{D}. \tag{6}$$

We emphasize that the absolute value of the diffusion length scale is not important here; we simply seek to characterize the qualitative segregation behavior during the growth of binary solid-solution crystals as a function of some dimensionless growth rate Γ_D. It should be further noted that the diffusion boundary layer constraint imposed by our simulation box size does not alter the overall physics of the problem; it merely allows us to isolate segregation behavior under constant growth conditions. Finally, note that the dimensionless quantity Γ_D is explicitly independent of MMC sweeps and therefore can be compared directly to an equivalent quantity obtained from BD simulations or experimental measurements. This issue will be addressed in detail in Sec. V.

B. MMC simulation of binary solid-solution colloidal crystals

Binary crystallization was simulated using the same overall protocol described in Sec. IV A. As mentioned earlier, the binary systems considered here are constructed so that $E_b^{AA} > E_b^{AB} > E_b^{BB}$. One experimental realization of a such a binary colloidal system is described in Ref. 12. Here, the difference in DNA strand sequence on the two sphere populations decreases the A-B bridge formation energy by $\Delta(\Delta G)$ relative to an A-A bridge so that

$$\frac{E_b^{AA}}{E_b^{AB}} = e^{(\Delta \Delta G / k_{\mathrm{B}} T)} \tag{7a}$$

and

$$\frac{E_b^{AA}}{E_b^{BB}} = e^{2(\Delta \Delta G / k_{\mathrm{B}} T)}. \tag{7b}$$

In order to provide control over the difference between the A-B and A-A interaction strengths, the system in Ref. 16 was engineered with spacer-linker sequence mismatches on both A and B particles. Two systems were created, where $\Delta(\Delta G)_1 \approx 0.22 k_{\mathrm{B}} T$ and $\Delta(\Delta G)_2 \approx 1.25 k_{\mathrm{B}} T$. The latter system exhibited almost total exclusion of B particles from the growing A crystal, while the first exhibited a substitution ratio of 0.092 ± 0.009 for crystallites grown from a suspension with 50:50 $A:B$ stoichiometry and 0.0154 ± 0.0025 for crystallites from a 90:10 $A:B$ suspension. The effective segregation coefficient (defined as the ratio of the fraction of impurity B particles in the crystal to that in the fluid) for both $A:B$ compositions was consistent with the value of $k_{\mathrm{seg}} = 0.18 \pm 0.02$.

All binary MMC simulations were equilibrated using pure A seeds containing 150 particles arranged in a fcc configuration and initialized with a fixed composition of particles within the overall simulation. In order to remove any bias imposed by this choice of initial seed composition, growth rate data were collected after over 1 ML of particles had been added to the seed. Also note that only particles added to the crystallite during the constant radial growth portion of the simulation were considered in the analysis. The properties of the A particles were used to define Γ_D for binary simulations so that $\Gamma_D = (dr/ds)\sigma/D_A$, where D_A is the bulk fluid diffusivity of A particles.[17] The binary segregation coefficient k_{seg} was computed across a large range of Γ_D values. To access different Γ_D values, a sequence of MMC runs was performed using different values of
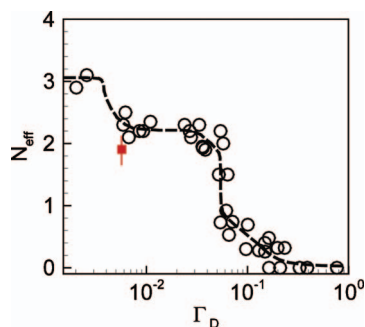
FIG. 4. Segregation behavior during binary crystallization of a solid solution as a function of scaled crystal growth rate (Γ_D). Open circles—MMC simulations for $\sigma=0.98$ μm and filled square—experimental measurement. The dashed line is a guide to the eye.

$E_b^{AA}(3.75k_BT-5.0k_BT)$, $E_b^{AB}(0.4k_BT\leq\Delta E_b\leq1.5k_BT)$, overall system volume fraction ($0.25<\phi<0.4$) and rd_{max} ($0.015\sigma<rd_{max}<0.06\sigma$).

In both experiment and simulation, the observed segregation coefficient can be interpreted in terms of the effective number of bonds N_{eff} with which an arriving particle equilibrates before becoming permanently attached to the growing crystal, i.e.,

$$k_{seg} = \exp\left(-\frac{N_{eff}\Delta E_b}{k_BT}\right). \tag{8}$$

Equation (8) can be analyzed as follows. Particles arriving at the surface of a growing crystal have a finite amount of time (established by the growth rate of the crystal) to reach equilibrium with the surface. This equilibration process depends on the nature of the interaction between the particle and the surface. For example, particles that form strong bonds to the surface (i.e., contacts with a large number of surface particles N) will require longer times to attach and detach enough instances to attain equilibrium with the surface. Thus, in Eq. (8), the apparent value of k_{seg} is determined by the slowest composition-altering process that can be equilibrated. In the fast growth limit, all particle equilibration processes are slow and the crystal composition is equivalent to the fluid phase composition, while for very slow growth, the crystal composition is determined by particles which possess the maximum number of particle-surface bonds. Note that the maximum number of bonds is a function of the surface morphology and is generally less than the bulk coordination number because bulk annealing is generally not possible in micron-scale colloidal crystals.

A plot of N_{eff} as a function of Γ_D for $\sigma=0.98$ μm particles reveals a single master curve, as shown in Fig. 4, regardless of what parameter values were used to generate a particular value of Γ_D. This result suggests that the segregation behavior is completely controlled by a competition between the growth rate and a process (or processes) whose rate is proportional to bulklike diffusion. Under slower growth conditions (relative to bulk diffusion), $\Gamma_D<0.2$, nonstoichiometric substitution is observed in which B particles are actively rejected relative to A particles at the growing crystal front. In the interval, $0.05<\Gamma_D<0.2$, N_{eff} rises rapidly as Γ_D decreases until reaching a plateau at $N_{eff}\sim2$. This

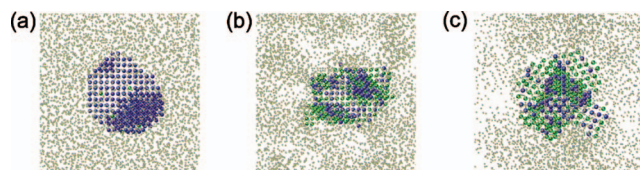FIG. 5. Snapshots showing MCM files of grown crystals at different values of Γ_D. (a) low Γ_D (~0.002), (b) intermediate Γ_D (~0.2), and (c) high Γ_D (~0.7). Simulation conditions for each of the three runs: (a) $\phi=0.3$, $E_b^{AA}=3.75k_BT$, and $\Delta E_b=1.25k_BT$; (b) $\phi=0.25$, $E_b^{AA}=6.0k_BT$, and $\Delta E_b=0.4k_BT$; and (c) $\phi=0.35$, $E_b^{AA}=6.0k_BT$, and $\Delta E_b=0.4k_BT$. All simulations contained particles with $\sigma=0.98$ μm at 50:50 A:B overall stoichiometry.

plateau extends across approximately one decade down to $\Gamma_D\sim0.003$, at which point N_{eff} once again rises rapidly to a value of approximately 3. Example configurations of grown crystallites are shown in Fig. 5 for various values of Γ_D. A final point regarding the data in Fig. 4 should be emphasized. The preferential incorporation of A particles into the crystal in general produces a compositional profile around the growing crystal, where the composition near the crystal surface is enhanced in B relative to the bulk. In the preceding analysis, we assume that such enhancement is small and that the bulk composition may be used to define the segregation coefficient. Manual analysis of several simulations shows that this assumption is valid over much of the parameters considered here.

Overall, our simulation results suggest that the segregation process is governed by the staircaselike hierarchy corresponding to different integer values of N_{eff} as Γ_D is varied. At high values of Γ_D (above ~0.2), $N_{eff}\sim0$, indicating fully nonequilibrium, stoichiometric growth (i.e., no rejection of particles by the growing crystal front). Note that although the crystal is fully stoichiometric (i.e., no segregation relative to the fluid composition) under these conditions, the crystal remains morphologically perfect, with no structural defect formation apparent, as shown in Fig. 5(b). The onset of the dendritic shape instability,[34] corresponding to the onset of morphological disturbances, is seen by $\Gamma_D\sim0.7$ [Fig. 5(c)]. Also shown in Fig. 4 is a data point generated from the experiments discussed above. The Γ_D value corresponding to the experimental conditions ($\Gamma_D\sim0.01$) was calculated by directly measuring the crystal growth rate ($\sim3\times10^{-4}$ μm/s) and correcting the bulk fluid diffusion coefficient to account for lubrication effects ($D_A\sim0.03$ μm/s^2). The latter arise because of hydrodynamic interactions between particles at low separation and are neglected in the MMC simulations. There is very good agreement between this experimental data point and the simulation predictions, although further studies will be required to fully validate the simulation results. Note that the careful control of crystal growth rate required to systematically probe other values of Γ_D with experiments is rather challenging.

While the discrete nature of the segregation process as a function of scaled growth rate is qualitatively understood in terms of an effective number of bonds controlling particle detachment, a still more quantitative picture can be formulated. Mechanistically, the time scale associated with detaching a particle from the crystallite surface can be decomposed into two contributions: first, the bonds between the particle
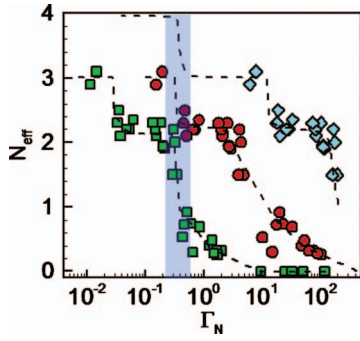
FIG. 6. N_{eff} as a function of Γ_2 (green squares), Γ_3 (red circles), and Γ_4 (cyan diamonds). The shaded region represents the transition area where Γ_N approaches unity for all N. Data shown correspond to $\sigma = 0.98$ μm particles.
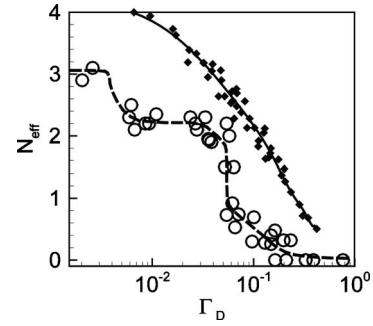

FIG. 7. Comparison of the binary colloidal (open circles) to atomistic (filled diamonds) (Ref. 24) segregation behavior. The atomistic segregation behavior is continuous compared to the kinetically limited integer segregation behavior of the binary macromolecule. The solid line is a polynomial fit to the atomistic data.

and the surface must be broken and, second, the particle has to diffuse sufficiently far away from the crystallite so that no memory of its excursion to the crystal is retained. The latter condition ensures that no correlation exists between a detachment and a subsequent attachment event. A simple model for these two sequential subprocesses can be expressed by

$$\tau_{diss}^N = \frac{L_W^2}{D_A} \exp\left(\frac{N E_b^{AA}}{k_B T} \right) + \frac{(2\sigma)^2}{D_A}, \qquad (9)$$

where L_W is the interaction length for the pair potential and N is the number of bonds that must be broken to free the particle under consideration. The bond-breaking time scale [first term in Eq. (9)] is assumed to be determined by the breaking of the strongest bonds, i.e., those between two A particles. The diffusion length scale employed in the second term in Eq. (9), 2σ, is approximately equal to the thickness over which fluid ordering is observed due to the crystal.

Using Eq. (9), a sequence of rescaled growth rates can then be defined as

$$\Gamma_N \equiv \tau_{diss}^N / \tau_{growth}, \qquad (10)$$

each of which compares the relative rates of crystal growth to a particular escape process defined by the number of bonds that must be broken to enable particle detachment from the crystal. In Fig. 7, the simulated value of N_{eff} is plotted against Γ_2, Γ_3, and Γ_4. Interestingly, the step transitions, $N_{eff}(\Gamma_2) = 1 \rightarrow 2$ and $N_{eff}(\Gamma_3) = 2 \rightarrow 3$, are now aligned at about $\Gamma_N \sim 1$. In other words, each step transition occurs when the corresponding Γ_N approaches unity. For example, as Γ_2 increases toward unity, the rate of the dissociation processes associated with the breakage of two bonds becomes comparable to the crystal growth rate, and equilibration of this process is no longer possible. At this point, $N_{eff}(\Gamma_2)$ is expected to decrease to a value below 2. Assuming that the faster one-bond dissociation process is still equilibrated, the observed N_{eff} value would be about 1, until $N_{eff}(\Gamma_1)$ becomes ~ 1, at which point a further decrease in N_{eff} would occur. Similar considerations apply for the entire hierarchy of dissociation processes. Note that no plateau is observed at $N_{eff} = 1$ because the diffusion time for particle escape is approximately equal to the time required for single bond breakage [see Eq. (9)]. The dashed line representing the transition $N_{eff}(\Gamma_4) = 3 \rightarrow 4$ shown in Fig. 6 is not based on the actual simulation data but represents the expected behavior from the present mechanistic model. Unfortunately, accessing simulation conditions corresponding to $N_{eff} = 4$ is too computationally expensive because of the extremely slow growth rates required.

C. Connections to segregation in atomic systems

In this section, the results from this work are compared to typical segregation behavior observed in atomic systems. Although the pair potential derived for the DNA-mediated system is qualitatively similar to that for simple atomic systems (e.g., a Lennard-Jones model for noble gases), key differences exist such as the interaction range and the shape of the soft-core repulsion. The former, in particular, is well known to drastically alter the phase diagram relative to atomic systems.[29] In order to draw a quantitative comparison between segregation behavior in our colloidal system and a typical atomistic one, we consider the work of Beatty and Jackson,[24,25] who define a rescaled crystal growth rate β as[25]

$$\beta = \frac{u \tau_C}{\sqrt{D \tau_C}}, \qquad (11)$$

where u is the crystal growth rate, τ_C is the average time it takes for a particle to join the crystal, and D is the diffusion coefficient of the bulk fluid. The time scale τ_C is chosen to be $\tau_C \sim \sigma^2 / D$ on the basis of similar arguments to those made in Sec. IV A; although the average diffusion distance to the growing crystal is not directly related to a single-particle diameter, we use this length scale only to allow us to make qualitative connections to the dimensionless growth rate introduced previously in Sec. IV A. The parameter β can be connected to Γ_D by noting that $u \sim dr/ds$ and $\tau_C \sim \sigma^2 / D$ so that $\beta \sim \Gamma_D$.

Our data are plotted along with the results of Beatty and Jackson for the tin-silicon binary system[24] in Fig. 7. In order to define corresponding N_{eff} values for the atomistic data, we assume that the value of the equilibrium segregation coefficient used in Ref. 24 ($k_{seg}^{eq} = 0.023$) corresponds to equilibrating the maximum possible number of bonds on the growing crystal surface. The latter value is taken to be approximately 4 for the growth of diamondlike crystals, which assumes that bulk reorganization is operational under equilibrium growth conditions. Applying Eq. (8) then gives an estimate for the
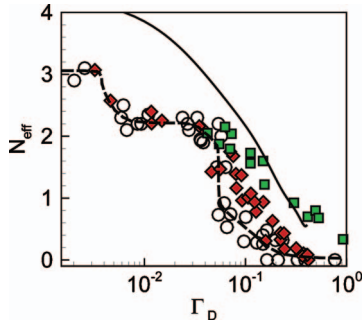
FIG. 8. Segregation behavior as a function of the colloid size for a fixed-range interparticle interaction potential. Dashed line and open circles—base case $\sigma=0.98$ μm; red diamonds—$\sigma=0.3$ μm; and green squares—$\sigma=0.1$ μm. The solid line represents a fit to the atomistic data in Ref. 24 for comparison.

parameter, $\Delta E_b \sim k_B T$, which was used to plot the data from Ref. 24 in Fig. 7. Notably, the atomistic segregation coefficient does not exhibit the stepped behavior predicted for the colloidal system although similar values of N_{eff} are apparent for equivalent scaled growth rates. The short-ranged nature of the colloidal interactions (at least for the particle sizes used in the present study) is therefore directly attributable to the steps in the N_{eff} curve. In the atomistic model, longer-ranged interactions effectively smear out the steps because approaching particles can form multiple bonds over a broad range of positions, whereas only very specific sites allow for multiple bond formation in the colloidal case.

We bridge our results for micron-sized colloidal particles to that for atomic systems by considering smaller colloidal particles. Additional binary crystallization simulations were performed with smaller microspheres ($\sigma=0.3$ and 0.1 μm), but with the same DNA oligomers used in the original system. Plots of N_{eff} against scaled growth rate for these two additional systems are shown in Fig. 8, along with the prior results for $\sigma=0.98$ μm. At $\sigma=0.3$ μm, the overall segregation is observed to still be somewhat stepped in nature but the steps between the integer values of N_{eff} are now more diffuse, particularly in the region where $0 \leq N_{\text{eff}} \leq 2$. The effect is even more pronounced for 0.1 μm diameter particles, although computational limitations prevent us from accessing N_{eff} values above 2. Nevertheless, for the 0.1 μm case, the evolution of the segregation behavior already appears to closely resemble that of an atomistic system. Note that for 0.1 μm diameter particles, the ratio of the interaction range to the particle diameter, L_W/σ, is still quite small (~ 0.3).

V. ANALYSIS OF MMC SIMULATION OF BD

In the remainder of this paper, we discuss the theoretical basis for connecting our MMC results to those from BD simulations. The theory for this connection is well established and proceeds via the Fokker–Planck equation (FPE).[35,36] In fact, the literature is replete with examples that demonstrate the applicability of MMC for simulating overdamped dynamics with applications to micromagnets,[37] classical magnetic moments,[38] protein chains,[39] and vacancy cluster diffusion.[40] In this section, we summarize the basic elements of this theory and use it to analyze the validity of

applying MMC to perform the studies presented in the preceding sections. In particular, we show that single-move MMC can offer significant computational advantages relative to BD simulations when applied to crystallization problems.

The temporal evolution of $P(X,t)$, the probability of a Markovian system residing in a state X at time t, is given by the Master equation

$$\frac{\partial P(X,t)}{\partial t} = \int \psi(X';\Delta X)P(X',t)d(\Delta X)$$
$$- \int \psi(X;\Delta X)P(X,t)d(\Delta X), \quad (12)$$

where $\psi(X;\Delta X)$ is the transition rate over a small but finite time interval Δt and $\Delta X \equiv X - X'$. For small ΔX, the Master equation can be approximated by a FPE of the form[41,42]

$$\frac{\partial P(X,t)}{\partial t} \approx -\frac{\partial}{\partial X}[A(X)P(X,t)] + \frac{1}{2}\frac{\partial^2}{\partial X^2}[B(X)P(X,t)], \quad (13a)$$

where

$$A(X) \equiv \int_{-\infty}^{\infty}(\Delta X)\psi(X;\Delta X)d(\Delta X) = \frac{\langle \Delta X \rangle}{\Delta t} \quad (13b)$$

and

$$B(X) \equiv \int_{-\infty}^{\infty}(\Delta X)^2\psi(X;\Delta X)d(\Delta X) = \frac{\langle (\Delta X)^2 \rangle}{\Delta t} \quad (13c)$$

are the drift and diffusion coefficients, respectively. Following Kikuchi et al.,[36] the drift and diffusion coefficients for the MMC "process" can be derived by direct substitution of the Metropolis criterion into Eqs. (13b) and (13c). For a proposed move in a one-dimensional system, the change in potential energy is $\Delta E = (\partial E/\partial X)\Delta X = (\partial E/\partial X)(rd_{\text{max}}\xi)$, where rd_{max} is the maximum displacement of the particle and ξ is a uniform random number in the interval $[-1,1]$. The mean displacement and mean square displacement over a number of MMC moves are given by[36]

$$\langle \Delta X \rangle = \sum_{\Delta X > 0}\frac{1}{Z}\Delta X + \sum_{\Delta X < 0}\frac{1}{Z}\exp\left(-\frac{1}{k_B T}\frac{\partial E}{\partial X}\Delta X\right)\Delta X, \quad (14)$$

$$\langle (\Delta X)^2 \rangle = \sum_{\Delta X > 0}\frac{1}{Z}(\Delta X)^2 + \sum_{\Delta X < 0}\frac{1}{Z}\exp\left(-\frac{1}{k_B T}\frac{\partial E}{\partial X}\Delta X\right)(\Delta X)^2, \quad (15)$$

respectively, where Z is a normalization factor that denotes the total finite number of possible states in a discretized system.

For sufficiently small ΔX, the exponential terms in Eqs. (14) and (15) can be expanded in powers of $\alpha \equiv (1/k_B T) \times (\partial E/\partial X)\Delta X$. Truncating the expansion to third order in α leads to the following expressions for the FPE drift and diffusion coefficients (see Appendix for the derivation):

$$A(X) = -\frac{1}{k_B T}\frac{\partial E}{\partial X}\frac{(rd_{max})^2}{6\Delta t} + \left(\frac{1}{k_B T}\frac{\partial E}{\partial X}\right)^2\frac{(rd_{max})^3}{16\Delta t} + O(rd_{max})^4,$$

(16)

$$B(X) = \frac{(rd_{max})^2}{3\Delta t} - \frac{1}{k_B T}\frac{\partial E}{\partial X}\frac{(rd_{max})^3}{8\Delta t} + O(rd_{max})^4.$$

(17)

Consider first the situation where $\alpha \ll 1$ and the first term in the expansion above is dominant. Under these conditions, the FPE [Eq. (13a)] suggests that $B(X)=2D$, or $D=(rd_{max})^2/6\Delta t$, which then implies that the drift coefficient is given by

$$A(X) \approx -\frac{D}{k_B T}\left(\frac{\partial E}{\partial X}\right) = -\frac{1}{\gamma}\left(\frac{\partial E}{\partial X}\right),$$

(18)

where the second equality in Eq. (18) makes use of the Einstein relation $D/k_B T = 1/\gamma$. The result in Eq. (18) is identical to the drift resulting from overdamped (diffusive) Langevin dynamics (with no hydrodynamic interactions present), as described in Ref. 42,

$$\gamma\frac{dX}{dt} = -\frac{dE}{dX} + R(t).$$

(19)

In other words, for sufficiently small $\Delta X = rd_{max}\xi$, the dynamics generated by MMC and solution of the inertialess Langevin equations are identical to within an underdetermined conversion factor between the number of MMC moves and time. Note that this equivalence is established on the scale of many MMC moves, i.e., long enough to establish the averages denoted in Eqs. (13)–(15).

As rd_{max} (and therefore ΔX) is increased, the convergence rate of the expansion applied to Eqs. (14) and (15) is reduced and additional terms become significant. Including additional terms within the expansions in Eqs. (16) and (17) implies that the drift and diffusion coefficients no longer are consistent with Langevin dynamics.[43,44] However, the ratio of the $(rd_{max})^3$ term to the $(rd_{max})^2$ term [in either Eq. (16) or Eq. (17)] gives a criterion for establishing the validity of MMC simulations of dynamical trajectories,

$$K \equiv \frac{3}{8}\frac{\partial E}{\partial X}\frac{rd_{max}}{k_B T} \ll 1.$$

(20)

In other words, only when $K \ll 1$ are MMC trajectories strictly consistent with BD (at a sufficiently coarse-grained time scale).

We validated the criterion in Eq. (20) by performing MMC simulations of cluster center-of-mass diffusion for isolated tetramers. It is well known that in the absence of hydrodynamic interactions, the Brownian diffusivity for a cluster of n particles is given by

$$\frac{D_{CM}}{D_{monomer}} = n^{-3/d},$$

(21)

where CM refers to the center-of-mass of the n-particle cluster and d is the dimension of the simulated system.[40,45] Shown in Fig. 9 is a plot of the cluster diffusivity scaled by the monomer diffusivity as a function of K for tetrahedrally configured tetramers bound by the DNA potential used in the
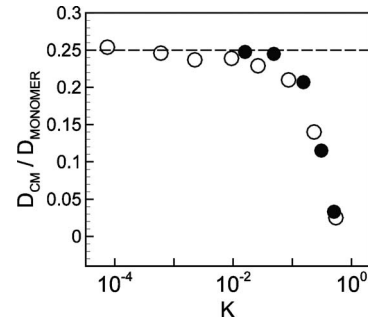

FIG. 9. Center-of-mass diffusion as a function of K for single (tetrahedrally configured) tetramer clusters, scaled by the monomer diffusivity. Open symbols—bead-spring model (Ref. 36) and filled symbols—DNA-mediated interactions. The horizontal dashed line corresponds to theoretical Brownian center-of-mass diffusivity for tetramer, scaled by monomer diffusivity.

previous sections ($\sigma=0.98$ μm). The value of K was obtained by averaging the gradient of the potential energy (calculated numerically as $\Delta E/\Delta X$ for each MMC move). The deviation from the expected Brownian behavior (dashed line) initiates at $K \sim 0.01-0.1$ and becomes progressively worse with increasing K, indicating that the criterion in Eq. (20) is, in fact, the relevant one, at least for cluster diffusion. Notably, cluster diffusion is almost completely arrested for K values approaching unity. Also shown in Fig. 9 are tetramer diffusion results for the bead-spring interaction model example employed in Ref. 36, which exhibits almost identical behavior.

Next, the averaged K values were calculated for the crystal growth MMC simulations presented earlier; these are shown in Fig. 10 for the $\sigma=0.98$ μm data, along with the corresponding N_{eff} versus Γ_D data. The resulting K values are distributed tightly in the range of $0.2 < K < 0.5$, with some even higher instances. Clearly, the MMC simulations were generally performed under conditions that do not satisfy the criterion in Eq. (20). On the other hand, also shown in Fig. 10 are the N_{eff} versus Γ_D data generated by BD and MD simulations for $\sigma=0.98$ μm microspheres. Note that the introduction of a scaled growth rate Γ_D allows for a direct comparison between the results of the two simulation methods because the MMC sweep/time factor cancels out in the definition of Γ_D. In the BD case, the friction coefficient, as well as binding energies and system volume fractions, were
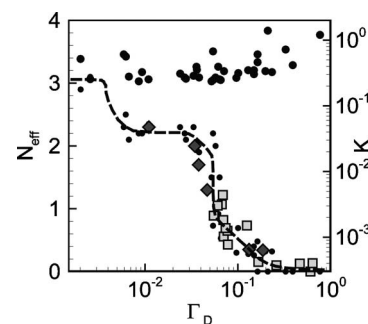

FIG. 10. Comparison of segregation behavior as a function of scaled growth rate during binary crystallization obtained from MMC (small filled circles), BD (squares), and MD (diamonds). Larger filled circles at top of figure represent the K value for each of the MMC data points. All runs correspond to $\sigma=0.98$ μm.
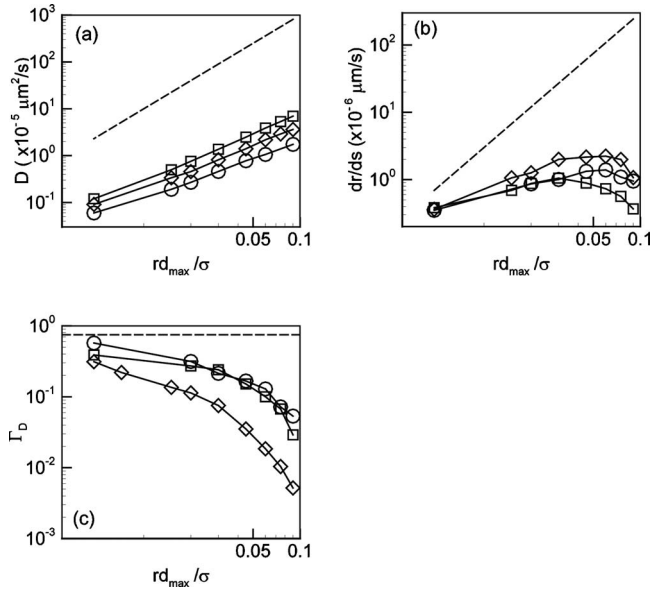
FIG. 11. The effect of rd_{max} on single-component bulk fluid diffusivity and crystal growth computed with MMC simulations of 0.98 μm diameter particles at a volume fraction of 30%. (a) Self-diffusion coefficient in a bulk fluid phase, (b) crystal growth rate, and (c) scaled growth rate, Γ_D. In all cases, $E_b = 3.75 k_B T$ (squares), $E_b = 4.25 k_B T$ (diamonds), and $E_b = 4.75 k_B T$ (circles). The dashed lines represent diffusion-limited conditions (see text).

adjusted to generate a range of Γ_D values, while only the latter was adjustable in the purely inertial MD case. Interestingly, the BD and MD data is statistically indistinguishable from the MMC data, although it was not possible to access very low values of Γ_D ($< 10^{-2}$) with either method. Moreover, the BD and MD runs at equivalent values of Γ_D were consistently slower than the MMC runs by up to factors of 10–20, making MMC simulation attractive for the present application.

The agreement between the BD, MD, and MMC data is at first somewhat surprising given the violation of the criterion in Eq. (20). To understand the apparent robustness of the master curve in Fig. 10, we consider the effect of varying the parameter rd_{max} on the basic processes taking place within the simulations: bulk fluid diffusion and crystal growth. Shown in Fig. 11 are plots of the dependence of the bulk fluid self-diffusivity, the crystal growth rate, and the resulting value of Γ_D on rd_{max} for three different binding energies in a single-component system. The bulk fluid diffusivity (defined in terms of MMC sweeps) in Fig. 11(a) increases with rd_{max} but slower than the expected $(rd_{max})^2$ scaling (dashed line). The deviation arises because of the high particle volume fraction (30%) which naturally reduces the self-diffusivity, and the fact that over much of the rd_{max} range considered, the small clusters that exist in the bulk fluid (in equilibrium with monomers) are artificially arrested due to increasing move rejection rate by the MMC method, as shown in Fig. 9. Note that the latter effect increases with increasing binding energy as expected from Eq. (20).

The crystal growth rate exhibits a more complex dependence on rd_{max}, in which it first increases and then decreases, for all binding energies. In the following, we establish a quantitative framework for analyzing these results by estimating the growth rate under purely diffusion-limited condi-

tions. Assuming a spherically symmetric crystal and diffusion-limited growth conditions, the growth rate of a crystal is given by

$$\frac{dn}{ds} = \frac{DC_0}{\sigma} A_{crys}, \tag{22}$$

where C_0 is the far-field (number) concentration of particles, A_{crys} is the crystal surface area, n is the number of particles in the crystal, and s is the number of MMC sweeps. In Eq. (22), it was assumed that the length scale of the diffusion profile around the growing cluster is on the order of σ, and the equilibrium fluid particle concentration at the cluster surface is small relative to C_0, consistent with a continuum interpretation of diffusion-limited growth.[46] Noting that $r_{crys} = (n/\phi_{crys})^{1/3}\sigma/2$, where r_{crys} is the crystal radius and ϕ_{crys} is the crystal volume fraction, Eq. (22) can be rewritten as

$$\frac{dr_{crys}}{ds} = \frac{\pi \sigma^2}{6 \phi_{crys}} D C_0 \sim \frac{\phi}{\phi_{crys} \sigma} D. \tag{23}$$

In other words, under diffusion-limited conditions, the radial growth rate is approximately of order the diffusion coefficient and scales as $(rd_{max})^2$. Equation (23) directly leads to the conclusion that

$$\Gamma_D = \frac{\phi}{\phi_{crys}}, \tag{24}$$

i.e., Γ_D is a constant of order unity under diffusion-limited growth conditions. Returning to Fig. 11(b), the actual growth rate observed for different binding energies is seen to diverge away from the diffusion-limited behavior (dashed line) with increasing rd_{max} and actually decreases for $rd_{max} > 0.05\sigma$. This decrease is readily attributable to the increasing fraction of particle attachment moves that are rejected by the MMC criterion. The combination of the effects shown in Figs. 11(a) and 11(b) lead directly to the results in Fig. 11(c), whereby the simulated values of Γ_D are seen to approach the diffusion-limited value as rd_{max} decreases.

The observations in Fig. 11 suggest an explanation for the robustness of the binary segregation behavior in Fig. 10 and more generally for the crystal growth process considered in this work. Given the absence of any specific energy barrier for particle attachment at the growing crystallite surface, we would expect that an overdamped, diffusion-dominated system (such as MMC) would predict that the crystal growth process operates in the diffusion-limited regime. This would indeed be the result for MMC simulations operating at very small rd_{max}, as suggested by Fig. 11(c). As rd_{max} is increased, deviation from diffusion-limited conditions arises because the increasing move rejection rate [i.e., the violation of the criterion in Eq. (20)] affects the bulk fluid self-diffusivity and the particle attachment/detachment processes at the crystal surface in different ways. The fact that the crystal growth rate is affected more strongly than the bulk self-diffusivity creates conditions that are akin to the presence of an attachment barrier at the crystal surface, i.e., these effects could be interpreted in terms of a surface reaction

limitation. The practical implication is that a larger range of dimensionless growth rates Γ_D can be accessed by varying the value of rd_{max}.

Similar arguments can be made regarding the BD and MD results. In order to access lower values of Γ_D in BD simulations, the effective solvent viscosity was lowered to about $\eta^* \sim 0.01$, where η^* is the solvent viscosity scaled by that of water. At these low values of solvent viscosity, BD simulations begin to exhibit inertial contributions in the particle trajectories and the attachment rate of particles at the crystal surface is decreased relative to the diffusion coefficient. In the MD limit, the particle motion is purely inertial and this effect is maximized. Simply put, whether the attachment rate relative to bulk diffusion is reduced by inertial effects or by unsuccessful MMC moves does not affect the segregation behavior. In other words, the phenomenon of interfacial segregation during crystal growth is completely determined by the relative rates of particle diffusion to and attachment/detachment at the crystal surface, and the exact mechanism by which these rates are established has essentially no bearing on the final result. Because we are only interested in the *relative* rates of these two processes for understanding segregation, we are unconstrained by the criterion in Eq. (20), keeping in mind that further increases in rd_{max} reduce the growth rate to impractically low levels.

In closing, we note an important limitation of running MMC simulations in the manner employed here. The above conclusions are only valid because the physics of the problem are dominated by single-particle processes. For example, in cases where cluster diffusion and coalescence are important, violation of Eq. (20) in a MMC simulation would lead to incorrect results relative to those obtained from BD. Conversely, the agreement between the three simulation methods over a wide range of parameters confirms the single-particle nature of the overall process. Of course, one should keep in mind that the BD simulations employed here and in many literature studies themselves are limited in describing cluster diffusion. The omission of hydrodynamic interactions in BD simulations leads to incorrect scaling with cluster size for the center-of-mass diffusivity, as shown in Eq. (21), which should be $D_{CM}(n) \sim n^{-1/d}$ instead.[47] Including such interactions dramatically increases the computational cost of direct simulation of crystal growth with the interaction models employed in this work.

VI. CONCLUSIONS

A detailed computational study was performed of binary crystallization in a colloidal system. The interparticle interactions employed in this work were specified by an analytical model that was validated by direct comparison to optical tweezer measurements, allowing for a quantitative comparison to experimental studies of binary crystallization. We find that the binary segregation behavior in the system can be described well by a simple model in which a hierarchy of interfacial processes, namely various types of particle detachments from the growth interface, competes with the overall growth rate of the crystal.

The observed segregation coefficient was found to ex-

hibit a stepped structure with respect to a dimensionless growth rate parameter, defined as the ratio of the crystal growth rate to the bulk fluid diffusivity. The stepped nature of the segregation behavior is a consequence of a separation between the rates of different particle detachment processes, which, in turn, results from the nature of the short-ranged DNA-mediated interactions (relative to the micron-scale spheres modeled here). Specifically, we find that surface particle detachment rates vary widely depending on the number of bonds formed with the crystal. The apparent segregation coefficient is then determined by the fastest detachment process that can still be equilibrated during crystal growth. For smaller particles, we find that the detachment rates become more closely spaced and the stepped nature of the apparent segregation coefficient gradually disappears, leading to the smoothly varying segregation behavior observed in atomic systems where the energy landscape at the crystal surface is smoothed by the longer-ranged interactions.

A key aspect of our study is the use of nonequilibrium MMC simulations to accelerate crystal growth relative to diffusion and access a broader range of growth conditions beyond what is possible with standard BD simulations. In order to do this, the MMC simulations were performed with moves that were large relative to the interaction distance (but small relative to the colloid scale). These operating conditions were shown mathematically to lead to some artifacts, but ones that were not relevant for the phenomenon under investigation. Specifically, it was shown that collective dynamics, such as cluster diffusion, were erroneously arrested in our simulations, but that these types of processes were unimportant in the context of the segregation behavior. In other words, we find that, at least relative to BD simulations, cluster diffusion and coalescence are not significant avenues for crystallization. Obviously, colloidal interactions at higher volume fractions will become increasingly dependent on collective particle motion.

ACKNOWLEDGMENTS

APPENDIX: MMC-BASED DRIFT AND DIFFUSION COEFFICIENTS FOR THE FPE

The change in potential energy for a MMC move is given by $\Delta E = (\partial E / \partial X) \Delta X = (\partial E / \partial X)(rd_{max}\xi)$, where ξ is a random number in the interval $[-1,1]$. Assuming that $\partial E / \partial X < 0$ (with no loss of generality), $\langle \Delta X \rangle$, and $\langle (\Delta X)^2 \rangle$ are given by

$$\langle \Delta X \rangle = \sum_{\Delta X > 0} \frac{1}{Z} \Delta X + \sum_{\Delta X < 0} \frac{1}{Z} \exp\left(-\frac{1}{k_B T} \frac{\partial E}{\partial X} \Delta X\right) \Delta X \qquad (A1)$$

and

$$\langle(\Delta X)^2\rangle = \sum_{\Delta X>0} \frac{1}{Z}(\Delta X)^2 + \sum_{\Delta X<0} \frac{1}{Z}\exp\left(-\frac{1}{k_BT}\frac{\partial E}{\partial X}\Delta X\right)(\Delta X)^2.$$

$$(A2)$$

Defining $\alpha \equiv (1/k_BT)(\partial E/\partial X)\Delta X = (1/k_BT)[\partial E/\partial X](rd_{max}\xi)$ and considering the small α limit gives

$$\langle\Delta X\rangle \approx \sum_{\Delta X>0} \frac{1}{Z}\Delta X + \sum_{\Delta X<0} \frac{1}{Z}\left(1-\alpha+\frac{\alpha^2}{2}\right)\Delta X + O(\Delta X)^4$$

$$\approx \frac{1}{Z}\left(\sum_{\Delta X>0}\Delta X + \sum_{\Delta X<0}\Delta X\right) + \sum_{\Delta X<0}\frac{1}{Z}\left(-\alpha+\frac{\alpha^2}{2}\right)\Delta X$$

$$+ O(\Delta X)^4.$$

$$(A3)$$

For constant $\partial E/\partial X$,

$$\langle\Delta X\rangle \approx -\frac{1}{k_BT}\frac{\partial E}{\partial X}(rd_{max})^2\sum_{\xi<0}\frac{\xi^2}{Z}$$

$$+ \left(\frac{1}{k_BT}\frac{\partial E}{\partial \chi}\right)^2\frac{(rd_{max})^3}{2}\sum_{\xi<0}\frac{\xi^3}{Z} + O(rd_{max})^4, \quad (A4)$$

and for small $|\xi|$ the summation over ξ can be expressed as an integral over $d\xi$ so that

$$\langle\Delta X\rangle \approx -\frac{1}{k_BT}\frac{\partial E}{\partial X}(rd_{max})^2\int_{\xi<0}\xi^2 d\xi$$

$$+ \left(\frac{1}{k_BT}\frac{\partial E}{\partial X}\right)^2\frac{(rd_{max})^3}{2}\int_{\xi<0}\xi^3 d\xi + O(rd_{max})^4.$$

$$(A5)$$

Evaluating the integrals in Eq. (A5) finally gives

$$\langle\Delta X\rangle \approx -\frac{1}{k_BT}\frac{\partial E}{\partial X}\frac{(rd_{max})^2}{6} + \left(\frac{1}{k_BT}\frac{\partial E}{\partial X}\right)^2\frac{(rd_{max})^3}{16}$$

$$+ O(rd_{max})^4.$$

$$(A6)$$

Similar considerations for Eq. (A2) give

$$\langle(\Delta X)^2\rangle \approx \left(\sum_{\Delta X>0}\frac{1}{Z}(\Delta X)^2 + \sum_{\Delta X<0}\frac{1}{Z}(\Delta X)^2\right)$$

$$- \sum_{\Delta X<0}\frac{\alpha}{Z}(\Delta X)^2 + O(\Delta X)^4, \quad (A7)$$

and for constant $\partial E/\partial X$ and small $|\xi|$,

$$\langle(\Delta X)^2\rangle \approx \frac{(rd_{max})^2}{3} - \frac{1}{k_BT}\frac{\partial E}{\partial X}\frac{(rd_{max})^3}{8} + O(rd_{max})^4. \quad (A8)$$

[1] U. Gasser, E. R. Weeks, A. Schofield, P. N. Pusey, and D. A. Weitz, Science **292**, 258 (2001).

[2] S. Auer and D. Frenkel, *Advanced Computer Simulation Approaches for Soft Matter Sciences I* (Springer, Berlin, 2005), Vol. 173, p. 149.

[3] Z. D. Cheng, W. B. Russell, and P. M. Chaikin, Nature (London) **401**, 443 (1999).

[4] A. M. Alsayed, M. F. Islam, J. Zhang, P. J. Collins, and A. G. Yodh, Science **309**, 1207 (2005); J. R. Savage, D. W. Blair, A. J. Levine, R. A. Guyer, and A. D. Dinsmore, *ibid.* **314**, 795 (2006).

[5] M. Prasad and T. Sinno, Phys. Rev. B **68**, 45206 (2003).

[6] M. Prasad and T. Sinno, Phys. Rev. B **68**, 45207 (2003).

[7] S. S. Kapur, M. Prasad, J. C. Crocker, and T. Sinno, Phys. Rev. B **72**, 014119 (2005).

[8] J. D. Joannopoulos, R. D. Meade, and J. N. Winn, *Photonic Crystals: Molding the Flow of Light* (Princeton University Press, Princeton, 1995).

[9] P. L. Biancaniello, A. J. Kim, and J. C. Crocker, Phys. Rev. Lett. **94**, 058302 (2005).

[10] D. Nykypanchuk, M. M. Maye, D. van der Lelie, and O. Gang, Langmuir **23**, 6305 (2007).

[11] H. Löwen, J. Phys.: Condens. Matter **13**, R415 (2001).

[12] A. J. Kim, P. L. Biancaniello, and J. C. Crocker, Langmuir **22**, 1991 (2006).

[13] M. E. Leunissen, C. G. Christova, A. P. Hynninen, C. P. Royall, A. I. Campbell, A. Imhof, M. Dijkstra, R. van Roij, and A. van Blaaderen, Nature (London) **437**, 235 (2005).

[14] D. Zerrouki, J. Baudry, D. Pine, P. Chaikin, and J. Bibette, Nature (London) **455**, 380 (2008).

[15] C. A. Mirkin, R. L. Letsinger, R. C. Mucic, and J. J. Storhoff, Nature (London) **382**, 607 (1996).

[16] A. J. Kim, thesis, University of Pennsylvania, 2006.

[17] A. J. Kim, R. Scarlett, P. L. Biancaniello, T. Sinno, and J. C. Crocker, Nature Mater. **8**, 52 (2009).

[18] D. Nykypanchuk, M. M. Maye, D. van der Lelie, and O. Gang, Nature (London) **451**, 549 (2008).

[19] S. Y. Park, A. K. R. Lytton-Jean, B. Lee, S. Weigand, G. C. Schatz, and C. A. Mirkin, Nature (London) **451**, 553 (2008).

[20] A. V. Tkachenko, Phys. Rev. Lett. **89**, 148303 (2002).

[21] C. F. Tejero, A. Daanoun, H. N. W. Lekkerkerker, and M. Baus, Phys. Rev. Lett. **73**, 752 (1994).

[22] V. N. Manoharan, M. T. Elsesser, and D. J. Pine, Science **301**, 483 (2003).

[23] S. C. Glotzer and M. J. Solomon, Nature Mater. **6**, 557 (2007).

[24] K. M. Beatty and K. A. Jackson, J. Cryst. Growth **271**, 495 (2004).

[25] K. A. Jackson, K. M. Beatty, and K. A. Gudgel, J. Cryst. Growth **271**, 481 (2004).

[26] D. B. Lukatsky, B. M. Mulder, and D. Frenkel, J. Phys.: Condens. Matter **18**, S567 (2006).

[27] N. A. Licata and A. V. Tkachenko, Phys. Rev. E **74**, 040401 (2006).

[28] R. Jullien, P. Jund, and D. Caprion, Phys. Rev. E **54**, 6035 (1996); W. S. Jodrey and E. M. Tory, Phys. Rev. A **32**, 2347 (1985).

[29] D. Frenkel, Physica A **313**, 1 (2002).

[30] P. J. Steinhardt, D. R. Nelson, and M. Ronchetti, Phys. Rev. B **28**, 784 (1983).

[31] P. R. ten Wolde and D. Frenkel, J. Chem. Phys. **109**, 9901 (1998).

[32] M. P. Allen and D. J. Tildesley, *Computer Simulation of Liquids* (Oxford University Press, New York, 1987).

[33] W. F. van Gunsteren and H. J. C. Berendsen, Mol. Phys. **45**, 637 (1982).

[34] W. W. Mullins and R. W. Sekerka, J. Appl. Phys. **34**, 323 (1963); **35**, 444 (1964); B. K. Johnson and R. F. Sekerka, Phys. Rev. E **52**, 6404 (1995).

[35] H. Risken, *The Fokker-Planck Equation*, 2nd ed. (Springer, Berlin, 1989).

[36] K. Kikuchi, M. Yoshida, T. Maekawa, and H. Watanabe, Chem. Phys. Lett. **185**, 335 (1991).

[37] X. Z. Cheng, M. B. A. Jalil, H. K. Lee, and Y. Okabe, Phys. Rev. Lett. **96**, 067208 (2006).

[38] U. Nowak, R. W. Chantrell, and E. C. Kennedy, Phys. Rev. Lett. **84**, 163 (2000).

[39] G. Tiana, L. Sutto, and R. A. Broglia, Physica A **380**, 241 (2007).

[40] S. V. Khare, N. C. Bartelt, and T. L. Einstein, Phys. Rev. Lett. **75**, 2148 (1995).

[41] R. K. Pathria, *Statistical Mechanics*, 2nd ed. (Elsevier Butterworth-Heinemann, Boston, 1996).

[42] N. G. v. Kampen, *Stochastic Processes in Physics and Chemistry* (Elsevier, Amsterdam, 2007).

[43] D. M. Heyes and A. C. Branka, Mol. Phys. **94**, 447 (1998).

[44] S. Whitelam and P. L. Geissler, J. Chem. Phys. **127**, 154101 (2007).

[45] A. F. Voter, Phys. Rev. B **34**, 6819 (1986).

[46] W. M. Deen, *Analysis of Transport Phenomena* (Oxford University Press, New York, 1998).

[47] A. W. C. Lau, B. D. Hoffman, A. Davies, J. C. Crocker, and T. C. Lubensky, Phys. Rev. Lett. **91**, 198101 (2003).